Transmission eigenchannels for coherent phonon transport

Transmission eigenchannels for coherent phonon transport

J. C. Klöckner,[1,2,*] J. C. Cuevas,[1,3] and F. Pauly[1,2]

[1]*Department of Physics, University of Konstanz, D-78457 Konstanz, Germany*

[2]*Okinawa Institute of Science and Technology Graduate University, Onna-son, Okinawa 904-0395, Japan*

[3]*Departamento de Física Teórica de la Materia Condensada and Condensed Matter Physics Center (IFIMAC), Universidad Autónoma de Madrid, E-28049 Madrid, Spain*

(Received 30 January 2018; revised manuscript received 11 April 2018; published 26 April 2018)

We present a procedure to determine transmission eigenchannels for coherent phonon transport in nanoscale devices using the framework of nonequilibrium Green's functions. We illustrate our procedure by analyzing a one-dimensional chain, where all steps can be carried out analytically. More importantly, we show how the procedure can be combined with *ab initio* calculations to provide a better understanding of phonon heat transport in realistic atomic-scale junctions. In particular, we study the phonon eigenchannels in a gold metallic atomic-size contact and different single-molecule junctions based on molecules such as an alkane chain, a brominated benzene-diamine, where destructive phonon interference effects take place, and a C_{60} junction.

DOI: 10.1103/PhysRevB.97.155432

I. INTRODUCTION

Recent advances in experimental techniques have enabled to explore the heat conduction in a great variety of nanoscale systems [1–4]. It has even become possible to measure the heat conductance of metallic wires all the way down to single-atom contacts [5,6], which constitute the ultimate limit of miniaturization of electronic and phononic systems. Research on heat conduction in nanoscale devices allows us to investigate the phonon transport in new regimes, where the theoretical description often requires fully atomistic approaches [7]. Here, we are especially interested in the theoretical analysis of phonon transport in atomic and molecular junctions, which are prototypical nanosystems that are studied intensely in the field of molecular electronics [8]. In these atomic-scale systems, the inelastic mean-free path for phonons is often much larger than the junction dimensions, and the phonon transport is therefore fully coherent. In this situation, the phonon transport is described within the framework of the Landauer-Büttiker scattering theory in which the contribution to the thermal conductance is determined by the elastic phonon transmission function of the system [8,9]. Different strategies have been put forward to compute this transmission function based on, for instance, the scattering matrix approach [10–14], mode-matching theory [15–17], or nonequilibrium Green's function (NEGF) techniques [18–27]. These approaches are nicely summarized in Ref. [28].

In the context of electronic transport, it has been shown that one can obtain a deep insight by resolving the total transmission $\tau = \sum_\mu \tau_\mu$ into contributions of eigenchannels, which are particular scattering states with transmission coefficients $0 \leqslant \tau_\mu \leqslant 1$. The analysis of the eigenchannels in metallic atomic-size contacts was crucial to elucidate the relation between the chemical valence of the atoms and the charge transport characteristics [29–32]. Furthermore, it has been shown that the electronic transmission coefficients of atomic contacts and molecular junctions can be determined experimentally with the help of superconductivity [31,33–35] or by measuring shot noise [36–41].

All this suggests that it would be important to carry out similar investigations in the case of coherent phonon transport. A related analysis to those of transmission eigenchannels is that of the mode-dependent transmission, which can be naturally performed with mode-matching-based approaches [15–17] or with the help of NEGF techniques [42,43]. However, mode-dependent transmission studies do not actually provide information on the eigenchannels in the central device part, and they are restricted to bulk systems with translational symmetry. For this reason, such a kind of analysis is not suitable for atomic and molecular junctions that lack spatial symmetry. Those atomic-scale systems are better described by means of a combination of *ab initio* methods and NEGF techniques [9]. The problem with NEGF-based approaches is that they do not provide immediate access to the scattering states on the central part of the system, which makes the determination of meaningful eigenchannels a challenging task. For this reason, the calculations performed with NEGF techniques are often interpreted with the help of the local density of states (LDOS) [44–47] rather than in terms of eigenchannels. Such analyses are certainly useful, but they do not provide a direct connection to the key quantity for coherent phonon transport, namely, the transmission function. Moreover, in those calculations the information about the phase gets lost, which is important, for instance, for the interpretation of interference effects. Instead, the eigenchannels are clearly connected to the transmission, they are also closely related to the local vibrational modes, and they preserve the information about the phase. In the case of electronic transport, Paulsson and Brandbyge [48] were able to establish a method as to how the eigenchannels can be obtained from information about the subspace of the central part of the device only, i.e., from data that are readily available

*jan.kloeckner@uni-konstanz.de

in NEGF-based approaches. The goal of this paper is to extend those ideas to obtain the eigenchannels for coherent phonon transport. In particular, we present here a general procedure to extract these eigenchannels in NEGF-based calculations. Moreover, we show that this formulation can be combined with state-of-the-art *ab initio* methods, and we illustrate its physical insight with the analysis of the phonon eigenchannels in a variety of single-atom and single-molecule junctions of special interest.

The rest of the paper is organized as follows. In Sec. II we present our procedure to determine transmission eigenchannels for coherent phonon transport in nanoscale systems. For this purpose, we introduce in Sec. II A the main equations to describe phonon transport, and we explain how they can be solved formally in terms of scattering states using NEGFs. In Sec. II B we discuss the spectral function, which plays a key role in the determination of the eigenchannels, and we show how it is connected to the scattering states of the system. Finally, in Sec. II C we present the procedure to determine the eigenchannels from a suitably chosen transmission probability matrix using only information about the subspace of the central part of the device. We illustrate this method in Sec. III through a detailed discussion of examples ranging from a simple toy model, consisting of a one-dimensional (1D) chain, to various realistic systems such as a gold atomic contact and single-molecule junctions based on an alkane chain, a benzene derivative, and a C_{60} molecule. We close the paper in Sec. IV with a brief summary of our main conclusions.

II. THEORETICAL PROCEDURE

In this section, we present the theoretical formalism to determine transmission eigenchannels for phonons. In analogy to electronic transport [48,49], we define the eigenchannel with number μ as particular scattering state that can be computed as the eigenfunction of a suitably chosen transmission probability matrix, while τ_μ is the corresponding transmission eigenvalue.

A. Scattering states

We start our analysis of the coherent phonon transport in a given nanoscale junction with the description of the phononic system in the harmonic approximation. Within this approximation, the phonons in an infinite spatial domain Ω are described by the following Hamiltonian:

$$\hat{H} = \sum_{i\in\Omega,\alpha} \frac{\hat{p}_{i\alpha}^2}{2} + \frac{1}{2\hbar^2} \sum_{i,j\in\Omega,\alpha,\beta} \hat{q}_{i\alpha} K_{i\alpha,j\beta} \hat{q}_{j\beta}. \tag{1}$$

Here, $\hat{q}_{i\alpha} = \hat{Q}_{i\alpha}\sqrt{m_i}$ is the mass-weighted displacement operator of atom i with mass m_i, $\hat{p}_{i\alpha} = \hat{P}_{i\alpha}/\sqrt{m_i}$ is the corresponding mass-scaled canonical momentum operator, and $K_{i\alpha,j\beta} = \hbar^2 \partial_{i\alpha}\partial_{j\beta} E_{\mathrm{BO}}/\sqrt{m_i m_j}$ is the dynamical matrix, which is the mass-weighted second derivative of the Born-Oppenheimer energy. Displacements of atoms i,j are assumed to be along the Cartesian axes $\alpha,\beta = x,y,z$. The operators in Eq. (1) fulfill the standard commutation relations $[\hat{q}_{i\alpha},\hat{q}_{j\beta}] = [\hat{p}_{i\alpha},\hat{p}_{j\beta}] = 0$ and $[\hat{q}_{i\alpha},\hat{p}_{j\beta}] = i\hbar\delta_{i,j}\delta_{\alpha,\beta}$.

In a typical transport setup, the domain Ω is divided into three parts: a semi-infinite left (L) lead, a finite central (C) part, and a semi-infinite right (R) lead. The Hamilton operator can then be written as

$$\hat{H} = \hat{H}_{\mathrm{L}} + \hat{H}_{\mathrm{C}} + \hat{H}_{\mathrm{R}}, \tag{2}$$

with

$$\hat{H}_X = \sum_{i\in X,\alpha} \frac{\hat{p}_{i\alpha}^2}{2} + \frac{1}{2\hbar^2} \sum_{i\in X,j\in\Omega,\alpha,\beta} \hat{q}_{i\alpha} K_{i\alpha,j\beta} \hat{q}_{j\beta}, \tag{3}$$

where $X = \mathrm{L,C,R}$. Since it is customary for phonon transport to work in the Heisenberg picture, we shall consider the Heisenberg operator

$$\hat{q}_{i\alpha}(t) = e^{i\hat{H}t/\hbar} \hat{q}_{i\alpha} e^{-i\hat{H}t/\hbar}. \tag{4}$$

It is straightforward to show that this operator fulfills the following equation of motion:

$$\hbar^2 \frac{d^2\hat{q}_{i\alpha}(t)}{dt^2} = -\sum_{j\in\Omega,\beta} K_{i\alpha,j\beta} \hat{q}_{j\beta}(t). \tag{5}$$

The full solution to this equation of motion is formed from two sets of states [50]. One set includes propagating states with a continuous energy spectrum. It is generated from the electrodes, which we assume to be perfect semi-infinite crystals without defects. The upper cutoff energy E_{c} of the spectrum is determined by the Debye energy of the left or right electrode material and is set to the maximum of the two values. The other set is formed by bound states with a discrete energy spectrum, originating from the finite central region. The bound states are not important for coherent transport because they do not contribute to the transmission. Nevertheless, we take them into account in our considerations since they are crucial for the normalization of the states, as we will discuss below.

The solution of Eq. (5) can then be expressed in terms of the normal modes of the propagating and bound sets as

$$\begin{aligned}\hat{q}_{i\alpha}(t) = &\int_0^{E_{\mathrm{c}}} dE \sum_m \frac{\hbar}{\sqrt{2E}} (b_m^\dagger(E)\Phi_{m,i\alpha}^*(E) e^{iEt/\hbar} + \mathrm{H.c.}) \\ &+ \sum_m \frac{\hbar}{\sqrt{2E_m}} (\bar{b}_m^\dagger \bar{\Phi}_{m,i\alpha}^* e^{iE_m t/\hbar} + \mathrm{H.c.}),\end{aligned} \tag{6}$$

where H.c. denotes Hermitian conjugation. The normal mode operators fulfill standard commutation relations with the only nonvanishing commutators being $[b_m(E),b_n^\dagger(E')] = \delta_{mn}\delta(E-E')$ and $[\bar{b}_m,\bar{b}_n^\dagger] = \delta_{mn}$. In these expressions, $\Phi_{m,i\alpha}(E)$ is the component of the normal mode vector $\mathbf{\Phi}_m(E)$ on atom i for the displacement along α, which solves the following eigenvalue problem:

$$K\mathbf{\Phi}_m(E) = E^2\mathbf{\Phi}_m(E) \tag{7}$$

for a given energy E. Here, m runs over all degenerate states with energy E. Similar relations hold for the bound states, where $\bar{\mathbf{\Phi}}_m$ is the normal mode vector m, which solves

$$K\bar{\mathbf{\Phi}}_m = E_m^2\bar{\mathbf{\Phi}}_m. \tag{8}$$

In this case, the index m enumerates all bound states. Overall, the normal mode vectors are normalized such that

$$\int_0^{E_c} dE \sum_m \mathbf{\Phi}^*_{m,i\alpha}(E)\mathbf{\Phi}_{m,j\beta}(E) + \sum_m \bar{\mathbf{\Phi}}^*_{m,i\alpha}\bar{\mathbf{\Phi}}_{m,j\beta} = \delta_{ij}\delta_{\alpha\beta}. \quad (9)$$

Since we are interested in the formulation of transport as a scattering problem, we solve Eq. (7) for the propagating set of states by starting from the solutions of the uncoupled subsystems X and treat the coupling between the different parts, K_{XY} with $Y \neq X$, as a perturbation K_1. For this reason we write $K = K_0 + K_1$ with

$$K_0 = \begin{pmatrix} K_{\mathrm{LL}} & 0 & 0 \\ 0 & K_{\mathrm{CC}} & 0 \\ 0 & 0 & K_{\mathrm{RR}} \end{pmatrix} \quad (10)$$

and

$$K_1 = \begin{pmatrix} 0 & K_{\mathrm{LC}} & 0 \\ K_{\mathrm{CL}} & 0 & K_{\mathrm{CR}} \\ 0 & K_{\mathrm{RC}} & 0 \end{pmatrix}. \quad (11)$$

Note that we assume here and henceforth that left and right parts are decoupled, meaning that $K_{\mathrm{LR}} = K^\dagger_{\mathrm{RL}} = 0$. For the eigenvalue E^2, we arrive in this way at a general solution $\mathbf{\Phi}_m(E) = (\mathbf{\Phi}_{m,\mathrm{L}}(E), \mathbf{\Phi}_{m,\mathrm{C}}(E), \mathbf{\Phi}_{m,\mathrm{R}}(E))^T$, which can be expressed by using the Green's function formalism as follows:

$$\mathbf{\Phi}_{m,X}(E) = \boldsymbol{\varphi}_{m,X}(E) + \sum_{Y\neq X} d^{\mathrm{r}}_{XX}(E)K_{XY}\mathbf{\Phi}_{m,Y}(E). \quad (12)$$

Here, $\boldsymbol{\varphi}_{m,X}(E)$ is the solution of the unperturbed system, i.e., $(E^2 - K_{XX})\boldsymbol{\varphi}_{m,X}(E) = 0$, and

$$d^{\mathrm{r}}_{XX}(E) = [(E+i\eta)^2 - K_{XX}]^{-1} \quad (13)$$

is the retarded Green's function of the unperturbed solution with an infinitesimal parameter $\eta > 0$. The states in Eq. (12) can also be written in terms of the retarded Green's function of the full system

$$D^{\mathrm{r}}(E) = [(E+i\eta)^2 - K]^{-1} \quad (14)$$

as

$$\mathbf{\Phi}_{m,X}(E) = \boldsymbol{\varphi}_{m,X}(E) + \sum_Z \sum_{Y\neq Z} D^{\mathrm{r}}_{XZ}(E)K_{ZY}\boldsymbol{\varphi}_{m,Y}(E). \quad (15)$$

From this equation, we define the scattering states $\mathbf{\Phi}^{\mathrm{L}}_m(E)$ [$\mathbf{\Phi}^{\mathrm{R}}_m(E)$] generated from unperturbed states that enter the junction region from the left (right) lead, which are special solutions with the boundary conditions $\boldsymbol{\varphi}_{m,\mathrm{C}}(E) = 0$ and simultaneously $\boldsymbol{\varphi}_{m,\mathrm{R}}(E) = 0$ [$\boldsymbol{\varphi}_{m,\mathrm{L}}(E) = 0$]. We will show in the next section that, apart from contributions due to bound states, these left- and right-incoming states give rise to the spectral function of the central part.

B. Spectral function

The phonon spectral function plays a central role in the determination of the transmission eigenchannels. This function is given in terms of the phonon Green's functions as follows:

$$A(E) = i\{D^{\mathrm{r}}(E) - [D^{\mathrm{r}}(E)]^\dagger\}. \quad (16)$$

Making use of the propagating and bound sets of solutions to Eqs. (7) and (8), the spectral function can be rewritten as

$$A(E) = -2\int_0^{E_c} dE' \sum_m \mathrm{Im}\left[\frac{\mathbf{\Phi}_m(E')\mathbf{\Phi}^\dagger_m(E')}{(E+i\eta)^2 - E'^2}\right] - 2\sum_m \mathrm{Im}\left[\frac{\bar{\mathbf{\Phi}}_m\bar{\mathbf{\Phi}}^\dagger_m}{(E+i\eta)^2 - E^2_m}\right]. \quad (17)$$

We note that this form of the spectral function is consistent with the standard definition of the Green's functions used for the derivation of the Landauer formula [19]. Those Green's functions are defined in terms of the operators $\hat{q}_{i\alpha}(t)$ of Eq. (6), and such a starting point also leads to Eq. (17). Now, using that $\lim_{\eta\to 0}\mathrm{Im}[1/(E+i\eta)] = -\pi\delta(E)$, we can express the spectral function as follows:

$$A(E) = \frac{\pi}{E}\sum_m \mathbf{\Phi}_m(E)\mathbf{\Phi}^\dagger_m(E) + \sum_m \frac{\pi}{E_m}\delta(E-E_m)\bar{\mathbf{\Phi}}_m\bar{\mathbf{\Phi}}^\dagger_m = \frac{\pi}{E}\rho(E), \quad (18)$$

where

$$\rho(E) = \sum_m \mathbf{\Phi}_m(E)\mathbf{\Phi}^\dagger_m(E) + \sum_m \delta(E-E_m)\bar{\mathbf{\Phi}}_m\bar{\mathbf{\Phi}}^\dagger_m \quad (19)$$

is the phonon density matrix. This shows that the sets of states $\mathbf{\Phi}_m(E)$ and $\bar{\mathbf{\Phi}}_m$, respectively, build up the density matrix at a given energy. From this expression the density of states of a given subset can be obtained by a projection on this subset and an additional trace over the respective degrees of freedom.

After these general considerations, we now address the spectral function of our scattering problem. We obtain the retarded Green's function in the central region from Eq. (14), and it is given by the Dyson equation

$$D^{\mathrm{r}}_{\mathrm{CC}}(E) = \left[(E+i\eta)^2 - K_{\mathrm{CC}} - \Pi^{\mathrm{r}}_{\mathrm{L}}(E) - \Pi^{\mathrm{r}}_{\mathrm{R}}(E)\right]^{-1}, \quad (20)$$

where $\Pi^{\mathrm{r}}_Z(E) = K_{\mathrm{C}Z}d^{\mathrm{r}}_{ZZ}(E)K_{Z\mathrm{C}}$ with $Z = \mathrm{L,R}$ is the embedding self-energy due to the coupling to the leads. The spectral function of the central part can then be expressed using Eq. (16) as

$$A_{\mathrm{C}}(E) = iD^{\mathrm{r}}_{\mathrm{CC}}(E)\left\{\left[D^{\mathrm{r}}_{\mathrm{CC}}(E)^\dagger\right]^{-1} - D^{\mathrm{r}}_{\mathrm{CC}}(E)^{-1}\right\}D^{\mathrm{r}}_{\mathrm{CC}}(E)^\dagger = \sum_{Z=\mathrm{L,R}} D^{\mathrm{r}}_{\mathrm{CC}}(E)\Lambda_Z(E)D^{\mathrm{r}}_{\mathrm{CC}}(E)^\dagger - 4i\eta E D^{\mathrm{r}}_{\mathrm{CC}}(E)D^{\mathrm{r}}_{\mathrm{CC}}(E)^\dagger \quad (21)$$

with $\Lambda_Z(E) = i[\Pi^{\mathrm{r}}_Z(E) - \Pi^{\mathrm{r}}_Z(E)^\dagger] = K_{\mathrm{C}Z}a_Z(E)K_{Z\mathrm{C}}$ and $a_Z(E) = (\pi/E)\sum_m \boldsymbol{\varphi}_{m,Z}(E)\boldsymbol{\varphi}^\dagger_{m,Z}(E)$. While the last term $-4i\eta E D^{\mathrm{r}}_{\mathrm{CC}}(E)D^{\mathrm{r}}_{\mathrm{CC}}(E)^\dagger$ in Eq. (21) corresponds to the bound-state contributions, one can show that the two terms $D^{\mathrm{r}}_{\mathrm{CC}}(E)\Lambda_Z(E)D^{\mathrm{r}}_{\mathrm{CC}}(E)^\dagger$ for $Z = \mathrm{L,R}$ are related to the scattering states $\mathbf{\Phi}^{\mathrm{L}}_m(E)$ and $\mathbf{\Phi}^{\mathrm{R}}_m(E)$. This can be demonstrated as

follows:

$$\begin{aligned} A_{\mathrm{C}}^{Z}(E) &= \frac{\pi}{E}\sum_{m} P_{\mathrm{C}}\boldsymbol{\Phi}_{m}^{Z}(E)\boldsymbol{\Phi}_{m}^{Z}(E)^{\dagger}P_{\mathrm{C}} \\ &= \frac{\pi}{E}\sum_{m} P_{\mathrm{C}}\big[\boldsymbol{\varphi}_{m}^{Z}(E) + D^{\mathrm{r}}(E)K_{1}\boldsymbol{\varphi}_{m}^{Z}(E)\big] \\ &\quad\times\big[\boldsymbol{\varphi}_{m}^{Z}(E)^{\dagger} + \boldsymbol{\varphi}_{m}^{Z}(E)^{\dagger}K_{1}^{\dagger}D^{\mathrm{r}}(E)^{\dagger}\big]P_{\mathrm{C}} \\ &= D_{\mathrm{CC}}^{\mathrm{r}}(E)\Lambda_{Z}(E)D_{\mathrm{CC}}^{\mathrm{r}}(E)^{\dagger}, \end{aligned} \tag{22}$$

where we have used Eq. (15) for the scattering states, $\boldsymbol{\varphi}_{m}^{\mathrm{L}}(E) = (\boldsymbol{\varphi}_{m,\mathrm{L}}(E),0,0)^{T}$, $\boldsymbol{\varphi}_{m}^{\mathrm{R}}(E) = (0,0,\boldsymbol{\varphi}_{m,\mathrm{R}}(E))^{T}$ and the projection operator

$$P_{\mathrm{C}} = \sum_{i\in\mathrm{C},\alpha} \boldsymbol{e}_{i\alpha}\boldsymbol{e}_{i\alpha}^{\dagger}. \tag{23}$$

In this expression, $\boldsymbol{e}_{i\alpha}$ is a unit vector of the same dimension as the $\boldsymbol{\Phi}_{m}(E)$, and its entries are given by $e_{i\alpha,j\beta} = \delta_{ij}\delta_{\alpha\beta}$. We have thus shown that the spectral function of the central part $A_{\mathrm{C}}(E) = A_{\mathrm{C}}^{\mathrm{L}}(E) + A_{\mathrm{C}}^{\mathrm{R}}(E) + A_{\mathrm{C}}^{\mathrm{B}}(E)$ consists of two spectral functions $A_{\mathrm{C}}^{\mathrm{L}}(E)$ and $A_{\mathrm{C}}^{\mathrm{R}}(E)$, which can be attributed to scattering states $\boldsymbol{\Phi}_{m}^{\mathrm{L}}(E)$ and $\boldsymbol{\Phi}_{m}^{\mathrm{R}}(E)$ that enter the central device region from the left and right leads, respectively, and a part $A_{\mathrm{C}}^{\mathrm{B}}(E)$ due to bound states.

C. Transmission eigenchannels

We are now in the position to finally describe the procedure to determine the transmission eigenchannels. Let us first recall that we assume that the left and right parts are decoupled [see Eqs. (10) and (11)]. Under these conditions and using the NEGF formalism, one can show that the phononic heat current is given by a Landauer-type formula that reads as [18,51–56]

$$J(T) = \frac{1}{2\pi\hbar}\int_{0}^{\infty} dE\, E\tau(E)[n_{\mathrm{R}}(E,T) - n_{\mathrm{L}}(E,T)], \tag{24}$$

where

$$\tau(E) = \mathrm{Tr}\big[D_{\mathrm{CC}}^{\mathrm{r}}(E)\Lambda_{\mathrm{L}}(E)D_{\mathrm{CC}}^{\mathrm{r}}(E)^{\dagger}\Lambda_{\mathrm{R}}(E)\big] \tag{25}$$

is the total phonon transmission and $n_{Z}(E,T) = 1/\{\exp[E/(k_{\mathrm{B}}T_{Z})] - 1\}$ is the Bose-Einstein distribution function.

In order to obtain eigenchannels as linear combinations of projections of scattering states onto the central junction part simultaneously with the corresponding transmission eigenvalues, we express the transmission using Eq. (22) with $Z = \mathrm{L}$ as

$$\begin{aligned} \tau(E) &= \mathrm{Tr}\big[A_{\mathrm{C}}^{\mathrm{L}}(E)\Lambda_{\mathrm{R}}(E)\big] \\ &= \frac{\pi}{E}\sum_{m} \boldsymbol{\Phi}_{m}^{\mathrm{L}}(E)^{\dagger}P_{\mathrm{C}}\Lambda_{\mathrm{R}}(E)P_{\mathrm{C}}\boldsymbol{\Phi}_{m}^{\mathrm{L}}(E). \end{aligned} \tag{26}$$

Inspired by this expression, we define the transmission probability matrix

$$\tau_{mn}^{(1)}(E) = \frac{\pi}{E}\boldsymbol{\Phi}_{m}^{\mathrm{L}}(E)^{\dagger}P_{\mathrm{C}}\Lambda_{\mathrm{R}}(E)P_{\mathrm{C}}\boldsymbol{\Phi}_{n}^{\mathrm{L}}(E), \tag{27}$$

which is actually the matrix that we shall diagonalize to obtain the eigenchannels.

In order to diagonalize this transmission matrix, we follow the procedure for the electronic problem, as described in Refs. [48,49], and perform a spectral decomposition for the central part of the spectral function

$$\begin{aligned} A_{\mathrm{C}}^{\mathrm{L}}(E) &= \sum_{m} \tilde{\boldsymbol{\chi}}_{m}(E)\lambda_{m}(E)\tilde{\boldsymbol{\chi}}_{m}^{\dagger}(E) \\ &= \frac{\pi}{E}\sum_{m} \tilde{\boldsymbol{\xi}}_{m}(E)\tilde{\boldsymbol{\xi}}_{m}^{\dagger}(E). \end{aligned} \tag{28}$$

Here, $\tilde{\boldsymbol{\xi}}_{m}(E) = \sqrt{E\lambda_{m}(E)/\pi}\,\tilde{\boldsymbol{\chi}}_{m}(E)$ and $\tilde{\boldsymbol{\chi}}_{m}^{\dagger}(E)\tilde{\boldsymbol{\chi}}_{n}(E) = \delta_{mn}$. As can be seen from a comparison of Eqs. (22) and (28), the vectors $\tilde{\boldsymbol{\xi}}_{m}(E) = P_{\mathrm{C}}\boldsymbol{\Phi}_{m}^{\mathrm{L}}(E)$ originate from the scattering states that arrive from the left lead via projections onto the central part and are therefore normalized through the $\boldsymbol{\Phi}_{m}^{\mathrm{L}}(E)$ [see also Eq. (9)]. Then, we transform $\pi\Lambda_{\mathrm{R}}(E)/E$ into the new basis of the $\tilde{\boldsymbol{\xi}}_{m}(E)$ through

$$\begin{aligned} \tau_{mn}^{(1)}(E) &= \frac{\pi}{E}\tilde{\boldsymbol{\xi}}_{m}^{\dagger}(E)\Lambda_{\mathrm{R}}(E)\tilde{\boldsymbol{\xi}}_{n}(E) \\ &= \frac{\pi}{E}[\tilde{U}^{\dagger}(E)\Lambda_{\mathrm{R}}(E)\tilde{U}(E)]_{mn}, \end{aligned} \tag{29}$$

where $\tilde{U}(E) = (\tilde{\boldsymbol{\xi}}_{1}(E),\ldots,\tilde{\boldsymbol{\xi}}_{3N_{\mathrm{C}}}(E))$ and N_{C} is the number of atoms in the central part. The eigenvectors are solutions of the equation

$$\sum_{n} \tau_{mn}^{(1)}(E)c_{n\mu}(E) = \tau_{\mu}(E)c_{m\mu}(E) \tag{30}$$

with $\sum_{m} c_{m\mu}^{*}(E)c_{m\nu}(E) = \delta_{\mu\nu}$, and the eigenchannel μ in the central region is given by

$$\begin{aligned} \tilde{\boldsymbol{\Psi}}_{\mu}(E) &= \sum_{m} c_{m\mu}(E)\tilde{\boldsymbol{\xi}}_{m}(E) \\ &= \sum_{i\in\mathrm{C},\alpha} a_{i\alpha,\mu}(E)\boldsymbol{e}_{i\alpha} \end{aligned} \tag{31}$$

with $a_{i\alpha,\mu}(E) = \sum_{m} \tilde{U}_{i\alpha,m}(E)c_{m\mu}(E)$. The eigenchannels thus arise from a unitary transformation of the states $\tilde{\boldsymbol{\xi}}_{m}(E)$.

Let us note that the eigenchannels of Eq. (31) are right eigenvectors of the transmission probability matrix $\tau^{(2)}(E) = A_{\mathrm{C}}^{\mathrm{L}}(E)\Lambda_{\mathrm{R}}(E)$ that appears in the trace of Eq. (26), i.e.,

$$\tau^{(2)}(E)\tilde{\boldsymbol{\Psi}}_{\mu}(E) = \tau_{\mu}(E)\tilde{\boldsymbol{\Psi}}_{\mu}(E). \tag{32}$$

This is evident, if the relations in Eqs. (28)–(31) are used. It is worth pointing out that apart from $\tau^{(1)}(E)$ or $\tau^{(2)}(E)$, one could eventually consider other forms for the transmission probability matrix. For instance, we might want to use $\tau^{(3)}(E) = t(E)t^{\dagger}(E)$ with $t(E) = \Lambda_{\mathrm{R}}^{1/2}(E)D_{\mathrm{CC}}^{\mathrm{r}}(E)\Lambda_{\mathrm{L}}^{1/2}(E)$. Given an eigenchannel $\tilde{\boldsymbol{\Psi}}_{\mu}(E)$ with eigenvalue $\tau_{\mu}(E)$ of $\tau^{(2)}(E)$ [see Eq. (32)], we find that $\Lambda_{\mathrm{R}}^{1/2}(E)\tilde{\boldsymbol{\Psi}}_{\mu}(E)$ is an eigenvector of $\tau^{(3)}(E)$ with the same eigenvalue $\tau_{\mu}(E)$. Similar to the electronic case [49], we thus observe that the eigenvectors of $\tau^{(3)}(E)$ do no longer result from a unitary transformation of scattering states that are projected onto the center via P_{C} [see Eq. (23)], as it was the case when using $\tau^{(2)}(E)$ [see Eq. (31)]. Instead, the matrix $\Lambda_{\mathrm{R}}^{1/2}(E)$ destroys simultaneously the P_{C} projection property as well as the normalization [see Eq. (9)], and a comparison of the amplitudes of eigenchannels of $\tau^{(3)}(E)$ would thus not be meaningful.

As it is obvious from the relation $\tilde{\boldsymbol{\xi}}_{m}(E) = P_{\mathrm{C}}\boldsymbol{\Phi}_{m}^{\mathrm{L}}(E)$, Eqs. (27)–(31) yield left-incoming eigenchannels originating from the scattering states $\boldsymbol{\Phi}_{m}^{\mathrm{L}}(E)$. This means that the

lattice vibrations arrive at the scattering region from the left lead and are subsequently transmitted to the right lead or scattered back to the left one. In order to obtain right-incoming eigenchannels, it is sufficient to start from $\tau^{(4)}_{mn}(E) = \pi \mathbf{\Phi}^{\mathrm{R}}_m(E)^\dagger P_{\mathrm{C}} \Lambda_{\mathrm{L}}(E) P_{\mathrm{C}} \mathbf{\Phi}^{\mathrm{R}}_n(E)/E$ in Eq. (27) or $\tau^{(5)}(E) = A^{\mathrm{R}}_{\mathrm{C}}(E)\Lambda_{\mathrm{L}}(E)$ in Eq. (32). The corresponding transmission probability matrices are obtained by rearranging the expression in the trace of Eq. (25) through cyclic permutation, by exploiting the definition of $A^{\mathrm{R}}_{\mathrm{C}}(E)$ in Eq. (22), and by noting that it can also be written in the form $A^{\mathrm{R}}_{\mathrm{C}}(E) = D^{\mathrm{r}}_{\mathrm{CC}}(E)^\dagger \Lambda_Z(E) D^{\mathrm{r}}_{\mathrm{CC}}(E)$ through the relations given in Eqs. (16) and (21).

The eigenchannels in the complete system space $\mathbf{\Psi}_\mu(E) = \sum_m c_{m\mu}(E)\mathbf{\Phi}^{\mathrm{L}}_m(E)$ can be obtained from the $\tilde{\mathbf{\Psi}}_\mu(E)$ in Eq. (31) by omitting the projection P_{C} on the central device part. We will, however, focus in the following on device-projected eigenchannels. The $\tilde{\mathbf{\Psi}}_\mu(E)$ are normalized according to Eq. (9) because they are constructed through a unitary transformation with the $c_{m\mu}$ from the $\tilde{\boldsymbol{\xi}}_m(E)$. Consequently, they are measured in units of $\mathrm{J}^{-1/2}$. There is also a global phase factor that needs to be fixed for every eigenchannel $\tilde{\mathbf{\Psi}}_\mu(E)$. In the examples shown below, we will simply set the component of a certain atom to a real value for the one-dimensional chain. In the *ab initio* calculations, the numerical routines used for computing the eigenvectors determine the phase factor, which may thus vary both with E and μ.

We want to transform now the $\tilde{\mathbf{\Psi}}_m(E)$ to displacement vectors measured in units of m, in analogy to what is done when normal modes of finite systems are calculated classically from the eigenvalue equation (8). For this reason, we divide $\tilde{\mathbf{\Psi}}_\mu(E)$ by $\sqrt{m_i}$ [see also the mass factor in Eq. (6)] and multiply in addition with an energy-dependent scaling factor $s(E)$ of unit $\mathrm{J}^{1/2}$ m. In this way, the complex displacements of the central part of the eigenchannels are obtained as

$$\begin{aligned}\tilde{\boldsymbol{Q}}_\mu(E) &= \sum_{i\in\mathrm{C},\alpha} \frac{s(E)}{\sqrt{m_i}} a_{i\alpha,\mu}(E)\boldsymbol{e}_{i\alpha} \\ &= \sum_{i\in\mathrm{C},\alpha} \frac{s(E)}{\sqrt{m_i}} |a_{i\alpha,\mu}(E)| e^{i\theta_{i\alpha,\mu}(E)}\boldsymbol{e}_{i\alpha}. \end{aligned} \tag{33}$$

Equation (33) shows that each atomic displacement acquires a phase factor due to the incident wave from the left lead. Note that the displacements of the eigenchannels $\tilde{\boldsymbol{Q}}_\mu(E)$ in Eq. (33) are proportional to the eigenchannels $\tilde{\mathbf{\Psi}}_\mu(E)$ in Eq. (31), if all of the m_i are the same, as it is the case in monoatomic junctions. In contrast, the proportionality is broken for heteroatomic junctions. We have furthermore introduced a real-valued scaling factor $s(E)$ in Eq. (33), which we may adjust for an optimized visualization of displacements at each energy E. In this way, eigenchannel displacements $\tilde{\boldsymbol{Q}}_\mu(E)$ at different energies should only be compared on qualitative grounds, while they are fully comparable at a certain fixed energy.

The full solution for a wave moving from left to right at an energy E is

$$\tilde{\boldsymbol{Q}}_\mu(t,E) = \tilde{\boldsymbol{Q}}_\mu(E) e^{-iEt/\hbar}. \tag{34}$$

Obviously, $\tilde{\boldsymbol{Q}}_\mu(t=0,E) = \tilde{\boldsymbol{Q}}_\mu(E)$. The time dependence of the real part of the eigenchannel displacement vector $\mathrm{Re}\,\tilde{\boldsymbol{Q}}_\mu(t,E)$ can be shown in a movie, and we refer the reader to the Supplemental Material for examples [57], which will be discussed in the next section. However, for illustrative purposes we shall often restrict ourselves in the following to the representation of the real part of the eigenchannel displacements at time $t = 0$, i.e., $\mathrm{Re}\,\tilde{\boldsymbol{Q}}_\mu(t=0,E) = \mathrm{Re}\,\tilde{\boldsymbol{Q}}_\mu(E)$.

III. EXAMPLES

We apply now the procedure described in the previous section to determine the phonon eigenchannels in different situations. The examples range from a one-dimensional chain, which can be solved analytically, to fully numerical cases of atomic and molecular junctions in three dimensions. The systems have been selected to show the versatility of the method, which is applicable to any system exhibiting phase-coherent phonon transport.

Let us also point out that in all cases studied below, we only present the results for the left-incoming eigenchannels since the junctions studied are rather symmetric. The right-incoming eigenchannels show a similar behavior and can be obtained at the same computational cost in an analogous procedure, as explained above.

A. 1D chain

We now consider the case of a 1D atomic chain, where the whole procedure for the determination of phonon transmission eigenchannels can be carried out analytically. The system that we are interested in is depicted in Fig. 1(a). In this model junction the C part consists of two atoms, labeled -1 and 0 and colored in black. These two atoms are coupled through a spring with force constant k_{c}. The leads are described by two semi-infinite chains of coupled harmonic oscillators with nearest-neighbor coupling constant k_{l}. The left (right) lead is connected to atom -1 (0) in the central region with a coupling constant k_{l}. Since the atomic movements are assumed to happen along the direction of the chain, α reduces to a single component, and the compound index $i\alpha$ simplifies to just the atom index i in the following. Furthermore, we assume that all atoms in the L, C, and R parts have the same mass $m_i = m$.

The Green's function of the central part $D^{\mathrm{r}}_{\mathrm{CC}}(E)$ can be obtained from Eq. (20) using

$$K_{\mathrm{CC}} = \begin{pmatrix} k_{\mathrm{c}}+k_{\mathrm{l}} & -k_{\mathrm{c}} \\ -k_{\mathrm{c}} & k_{\mathrm{c}}+k_{\mathrm{l}} \end{pmatrix} \tag{35}$$

together with the self-energies

$$\Pi^{\mathrm{r}}_{\mathrm{L}}(E) = f(E)\begin{pmatrix}1&0\\0&0\end{pmatrix}, \quad \Pi^{\mathrm{r}}_{\mathrm{R}}(E) = f(E)\begin{pmatrix}0&0\\0&1\end{pmatrix}, \tag{36}$$

where $f(E) = (E^2 - 2k_{\mathrm{l}} - E\sqrt{E^2-4k_{\mathrm{l}}})/2$. Thus, the corresponding linewidth-broadening matrices can be written as

$$\Lambda_{\mathrm{L}}(E) = g(E)\begin{pmatrix}1&0\\0&0\end{pmatrix}, \quad \Lambda_{\mathrm{R}}(E) = g(E)\begin{pmatrix}0&0\\0&1\end{pmatrix}, \tag{37}$$

with

$$g(E) = \begin{cases} E\sqrt{4k_{\mathrm{l}} - E^2} & \text{if } E^2 < 4k_{\mathrm{l}}, \\ 0 & \text{if } E^2 \geqslant 4k_{\mathrm{l}}. \end{cases} \tag{38}$$

From these expressions, the spectral function $A^{\mathrm{L}}_{\mathrm{C}}(E)$ in Eqs. (22) and (28) is computed. For $E^2 < 4k_{\mathrm{l}}$, the eigenvalues

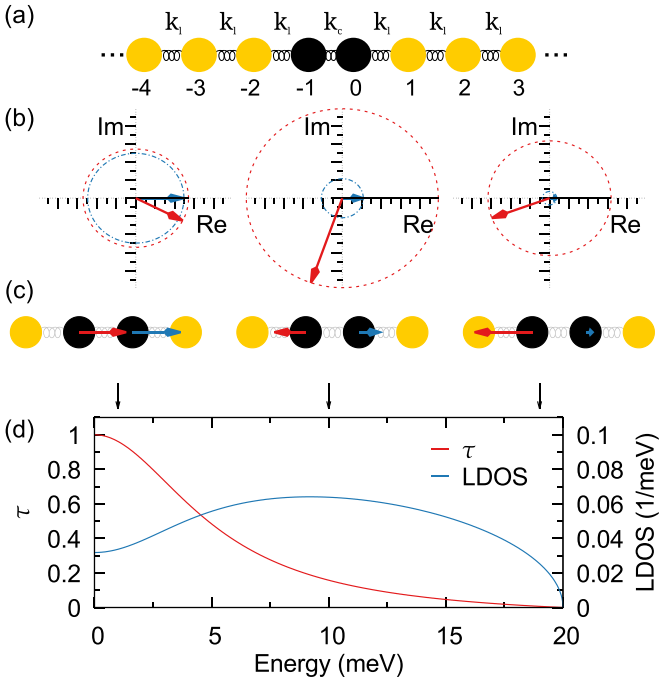

FIG. 1. (a) Sketch of the 1D junction. Two semi-infinite leads with nearest-neighbor coupling constants k_l are connected at sites -1 and 0 with the coupling constant k_c. The region $(-\infty, -2]$ is considered as the L part, the region $[-1,0]$ as the C part, and $[1,\infty)$ as the R part. (b) Transmission eigenchannel $\tilde{\boldsymbol{Q}}_1(E,t=0)$ for the 1D chain represented in the complex plane for energies of $E = 1$, 10, and 19 meV. The red arrow shows the complex number $\tilde{Q}_{1,-1}(E,t=0)$ for the atom -1, the blue one $\tilde{Q}_{1,0}(E,t=0)$ for atom 0. (c) The same as in (b), but now we display only the real part of the solution $\mathrm{Re}\,\tilde{\boldsymbol{Q}}_1(E,t=0)$. (d) The corresponding transmission eigenvalue $\tau_1(E)$ as a function of energy together with the LDOS of one of the atoms (-1 or 0) in the central part. The energies of those eigenchannels, which are studied in (b) and (c), are indicated with arrows. For (b)–(d), we assumed spring constants of $k_l = 100$ meV^2 and $k_c = 20$ meV^2.

of this matrix are given by

$$\lambda_1(E) = \frac{\sqrt{4k_l - E^2}\left[2k_c^2 + E^2(k_l - k_c)\right]}{k_l E\left[4k_c^2 + E^2(k_l - 2k_c)\right]}, \quad \lambda_2(E) = 0 \tag{39}$$

with the corresponding eigenvectors

$$\tilde{\boldsymbol{\chi}}_1(E) = \begin{pmatrix} \frac{-E^2+2k_c-iE\sqrt{4k_l-E^2}}{\sqrt{8k_c^2+4E^2(k_l-k_c)}} \\ \frac{k_c}{\sqrt{2k_c^2+E^2(k_l-k_c)}} \end{pmatrix},$$

$$\tilde{\boldsymbol{\chi}}_2(E) = \begin{pmatrix} \frac{k_c(E^2-2k_c+iE\sqrt{4k_l-E^2})}{2\sqrt{[k_c^2+E^2(k_l-k_c)][2k_c^2+E^2(k_l-k_c)]}} \\ \frac{\sqrt{k_c^2+E^2(k_l-k_c)}}{\sqrt{2k_c^2+E^2(k_l-k_c)}} \end{pmatrix}, \tag{40}$$

which are orthonormal, i.e., $\tilde{\boldsymbol{\chi}}_m^\dagger(E)\tilde{\boldsymbol{\chi}}_n(E) = \delta_{mn}$. From the $\tilde{\boldsymbol{\chi}}_m(E)$ we obtain the C projections of left-incoming scattering states $\tilde{\boldsymbol{\xi}}_m(E)$ by multiplying with $\sqrt{E\lambda_m(E)/\pi}$ [see the discussion of Eq. (28)]. Constructing $\tilde{U}(E) = (\tilde{\boldsymbol{\xi}}_1(E), \tilde{\boldsymbol{\xi}}_2(E))$, we determine $\tau^{(1)}(E)$ via Eq. (29). Diagonalizing the resulting transmission probability matrix [see Eq. (30)], we obtain the transmission eigenvalues

$$\tau_1(E) = \frac{k_c^2(4k_l - E^2)}{k_l\left[4k_c^2 + E^2(k_l - 2k_c)\right]}, \quad \tau_2(E) = 0 \tag{41}$$

and eigenvectors

$$\boldsymbol{c}_1(E) = \begin{pmatrix} 1 \\ 0 \end{pmatrix}, \quad \boldsymbol{c}_2(E) = \begin{pmatrix} 0 \\ 1 \end{pmatrix}. \tag{42}$$

These coefficients determine the eigenchannels $\tilde{\boldsymbol{\Psi}}_\mu(E)$ via Eq. (31). The time-dependent eigenchannel displacements can now be computed through Eqs. (33) and (34) by transforming the eigenchannels to the eigenchannel displacement vectors and by multiplying with a time-dependent phase factor.

Since we assume that the masses of all atoms $m_i = m$ are identical in the 1D chain, eigenchannels and eigenchannel displacements are proportional $\tilde{\boldsymbol{Q}}_\mu(E) = s(E)\tilde{\boldsymbol{\Psi}}_\mu(E)/\sqrt{m}$ to each other. We therefore define $\tilde{\boldsymbol{\Psi}}_\mu(E,t) = \sqrt{m}\,\tilde{\boldsymbol{Q}}_\mu(t,E)/s(E)$ and use both quantities interchangeably. Choosing the global phase factor of the eigenchannel such that the component of the atom 0 is real and positive at $t = 0$, the time-dependent eigenchannels read as

$$\tilde{\boldsymbol{\Psi}}_1(t,E) = \sqrt{\frac{\sqrt{4k_l - E^2}k_c^2}{\pi k_l\left[E^2(k_l - 2k_c) + 4k_c^2\right]}} \times \begin{pmatrix} \frac{-E^2+2k_c-iE\sqrt{4k_l-E^2}}{2k_c} \\ 1 \end{pmatrix} e^{-iEt/\hbar}, \quad \tilde{\boldsymbol{\Psi}}_2(t,E) = 0. \tag{43}$$

Let us discuss several points at this stage. We note that there is only a single eigenchannel with nonvanishing transmission. This is due to the fact that in our 1D model there is only nearest-neighbor coupling. Displacements, which we assume to be along the chain direction, thus need to spread sequentially from atom to atom. The leads provide a cutoff energy of $E_c = 2\sqrt{k_l}$, above which no propagating states exist. If $0 \leqslant k_c \leqslant k_l$ the whole junction shows no bound states, while they arise if $k_c > k_l \geqslant 0$. Due to the particular left-right symmetry of our problem, the following relations hold for $k_c \leqslant k_l$: $\rho_{ii}(E) = E[A_{ii}^{\mathrm{L}}(E) + A_{ii}^{\mathrm{R}}(E)]/\pi = E\,\mathrm{Tr}[A_{\mathrm{C}}^{\mathrm{L}}(E)]/\pi = E\lambda_1(E)/\pi = |\tilde{\boldsymbol{\Psi}}_1(E)|^2$ with $i = -1, 0$. The expressions imply that the square of the norm of the transmission eigenchannel 1 follows the LDOS of one of the atoms in the C part. Integration yields $\int_0^{E_c} dE\rho_{ii}(E) = \int_0^{E_c} dE|\tilde{\boldsymbol{\Psi}}_1(E)|^2 = 1$, which is consistent with the normalization condition in Eq. (9) since there are no bound states present. For the case $k_c > k_l$, we get $\int_0^{E_c} dE|\tilde{\boldsymbol{\Psi}}_1(E)|^2 < 1$, and bound-state contributions need to be taken into account in the C part to fulfill the normalization condition in Eq. (9).

If we now consider the perfect chain with $k_c = k_l$, the previous results reduce to

$$\tau_1(E) = 1, \quad \tau_2(E) = 0 \tag{44}$$

with

$$\tilde{\boldsymbol{\Psi}}_1(t,E) = \frac{1}{\sqrt{\pi\sqrt{4k_l - E^2}}}\begin{pmatrix} u_{-1}(t,E) \\ u_0(t,E) \end{pmatrix}, \quad \tilde{\boldsymbol{\Psi}}_2(t,E) = 0, \tag{45}$$

where $u_n(t,E) = \exp[ik(E)nd - iEt/\hbar]$. The $u_n(t,E)$ appear as solutions for the equation of motion of atoms arranged in an infinite chain and coupled by the same nearest-neighbor spring constants [58]. Here, we have introduced the wave vector $k(E) = (2/d)\sin^{-1}(E/E_c)$ and neighboring atoms are assumed to be separated by the distance d. Note that the interatomic distance d is not relevant for our transport problem, which is entirely determined by the force constant matrix K [see Eqs. (10) and (11)], where force constants will of course be functions of interatomic distances in realistic systems. As discussed in the previous paragraph, we find that $\rho_{ii}(E) = |\tilde{\mathbf{\Psi}}_1(E)|^2 = 2/(\pi\sqrt{4k_l - E^2})$ with $\int_0^{E_c} dE\, \rho_{ii}(E) = 1$.

We want to use now the analytical expressions to examine different representations of the transmission eigenchannel displacements. For this purpose we choose the global scaling factor $s/\sqrt{m}$ in Eq. (33) to be real, energy independent, and of units $\mathrm{J}^{1/2}\,\mathrm{m/kg}^{1/2}$. In Figs. 1(b)–1(d) we study the transmission, LDOS, and eigenchannel displacements for the 1D chain with $k_l = 100$ meV^2 and $k_c = 20$ meV^2, i.e., in the situation where there are only propagating states in the junction system. Corresponding figures for the perfect chain with $k_c = k_l = 100$ meV^2 and with bound-states contributions $k_l = 100$ meV^2 and $k_c = 2000$ meV^2 can be found in the Supplemental Material [57]. The transmission $\tau(E)$ in Fig. 1(d) shows a monotonically decreasing behavior with increasing energy and vanishes above the cutoff energy of $E_c = 20$ meV. At the same time, we plot the LDOS $\rho_{ii}(E)$ of the atom $i = -1,0$ in the central part, which starts from a finite value at $E = 0$, increases to a maximum around 9 meV and drops to zero beyond E_c. The transmission eigenchannel displacements $\tilde{\mathbf{Q}}_1(t = 0,E)$ are shown in Fig. 1(b) for the energies $E = 1, 10$, and 19 meV, indicated by arrows in Fig. 1(d). The two complex components are indicated by two arrows in the complex plane. Notice that while the norm of the eigenvector $\tilde{\mathbf{Q}}_1(t,E)$ is proportional to $\sqrt{\rho_{ii}(E)}$ for the energy-independent s chosen here, the relative magnitude at the atom $i = 0$ as compared to the atom $i = -1$, i.e., $|\tilde{Q}_{1,0}(t,E)|/|\tilde{Q}_{1,-1}(t,E)|$, decreases with increasing energy because a larger portion of the left-incoming wave gets reflected at the constriction. We also note that the phase difference $\theta_{0,1}(E) - \theta_{-1,1}(E)$ [see Eq. (33)] between the two components increases from 0 at $E = 0$ to π at $E = 20$ meV. With increasing time the arrows precess around the origin at a constant angular velocity of $\omega = E/\hbar$, spanning the circle indicated by the dashed lines in the plot. Since the two atoms typically do not swing in phase, the real parts of $\tilde{Q}_{1,-1}(t,E)$ and $\tilde{Q}_{1,0}(t,E)$ take maximum amplitudes at different times.

In Fig. 1(c) we present another way to visualize the eigenchannel displacements by simply plotting $\mathrm{Re}\,\tilde{Q}_{1,-1}(t,E)$ and $\mathrm{Re}\,\tilde{Q}_{1,0}(t,E)$ at $t = 0$ as arrows attached to the respective atoms. This is actually the representation that we will use in all the figures shown in the rest of the paper. Notice that due to our choice of the global phase factor, we get $\theta_{0,1}(E) = 0$ and $\mathrm{Re}\,\tilde{Q}_{1,0}(t = 0,E)$ is hence maximal at $t = 0$. In contrast, $\mathrm{Re}\,\tilde{Q}_{1,-1}(t,E)$ depends both on the absolute value $|\tilde{Q}_{1,-1}(E)|$ and the phase $\theta_{-1,1}(E)$, as it is visible from Fig. 1(b). Despite the large $|\tilde{Q}_{1,-1}(E)|$ at $E = 10$ meV, $\mathrm{Re}\,\tilde{Q}_{1,-1}(t,E)$ is rather small because $\theta_{-1,1}(E) \approx -0.6\pi$. In spite of such shortcomings, one gets an impression of the nature of the atomic motions involved in the eigenchannel. Indeed, we observe that the eigenchannel displacements at low energy $E = 1$ meV resemble a translational mode of the two atoms, while they are basically vibrating against each other at 19 meV, as it is clear from the evolution of the phase difference $\theta_{0,1}(E) - \theta_{-1,1}(E)$ with energy, discussed in the previous paragraph. Videos could be used to examine the full time-dependent dynamics of $\mathrm{Re}\,\tilde{\mathbf{Q}}_1(t,E)$, but we refrain from this here since the simple 1D case is well characterized with the help of Fig. 1(b).

B. *Ab initio* results

After illustrating the method with the simple 1D model, we apply it now to realistic systems. In these systems, we determine the force constant matrix for a particular junction geometry with the help of density functional theory (DFT) and describe the coherent phonon transport within the NEGF formalism explained in Sec. II. In particular, we will present different examples of the analysis of the phonon eigenchannels in nanoscale systems that include a gold single-atom contact [59] and several single-molecule junctions made of gold electrodes that are bridged by an alkane chain [60], a benzene ring with a bromine substituent [61], where destructive interference effects show up, and a C_{60} molecule [62]. Let us stress that we have already studied in detail the phononic thermal conductance in these systems in the references cited above. Here, we shall focus on the new insight provided by the analysis of the eigenchannels, and we refer the reader to those publications for the technical details on the calculations of the transmission functions.

In our junctions with gold electrodes, the Debye energy of the metal of around 20 meV represents the cutoff energy for the propagating states of the scattering problem. Because gas-phase molecules typically show vibrations with energies much above E_c, this leads to bound states in the molecular junctions. They need to be considered for a proper normalization of the eigenchannels $\tilde{\mathbf{\Psi}}_\mu(E)$ in Eq. (31).

We visualize eigenchannels in all the figures below in terms of the static picture of the real part of the eigenchannel displacements at $t = 0$, i.e., $\mathrm{Re}\,\tilde{\mathbf{Q}}_\mu(t = 0,E) = \mathrm{Re}\,\tilde{\mathbf{Q}}_\mu(E)$ [see Eqs. (33) and (34)], but we illustrate the real part of the full time-dependent solutions $\mathrm{Re}\,\tilde{\mathbf{Q}}_\mu(t,E)$ in the form of movies online [57]. In contrast to the 1D model, the masses of the atoms m_i are different in the heteroatomic molecular junctions. This leads to the fact that the eigenchannel displacements $\tilde{\mathbf{Q}}_\mu(E)$ are no longer proportional to the eigenchannels $\tilde{\mathbf{\Psi}}_\mu(E)$. Below, we will adjust the real-valued scaling factor $s(E)$ of Eq. (33) for an optimized visualization of eigenchannel displacements at each energy E. In this way, the vectors $\mathrm{Re}\,\tilde{\mathbf{Q}}_\mu(E)$ at different energies should only be compared on qualitative grounds, while they are fully comparable at a certain fixed energy. Since it should be obvious in which situation we mean the genuine eigenchannels $\tilde{\mathbf{\Psi}}_\mu(E)$ as compared to the eigenchannel displacements $\tilde{\mathbf{Q}}_\mu(E)$, we do not clearly distinguish them anymore and often simply refer to both as "eigenchannels" in the following. For convenience, we will henceforth furthermore omit all energy arguments.

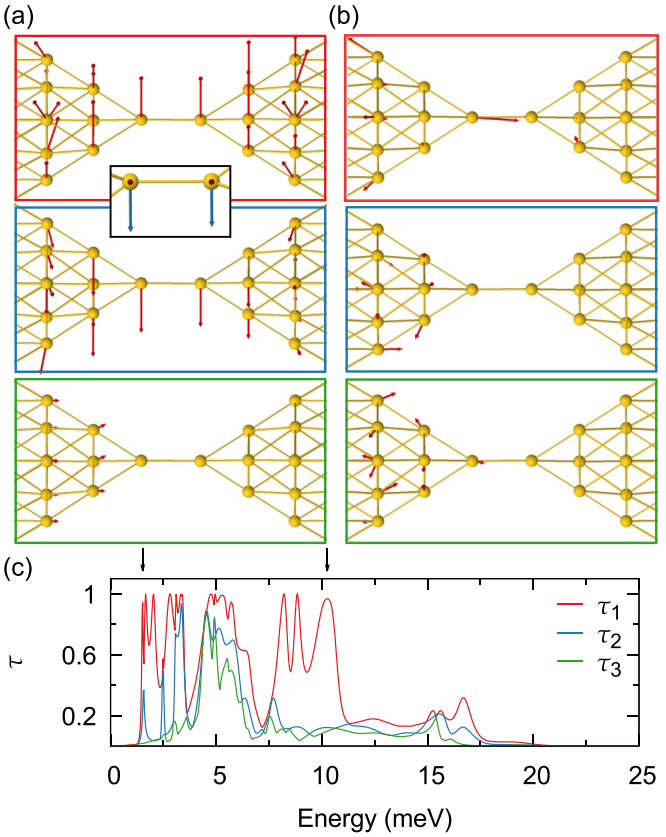

FIG. 2. (a) Transmission eigenchannels for a gold dimer contact at an energy of 1.5 meV. We show the three eigenchannels with the highest transmissions, which are equal to $\tau_1 = 0.943$, $\tau_2 = 0.238$ and $\tau_3 = 0.002$. To better visualize the perpendicular polarizations of eigenchannels 1 and 2, we have inserted an inset between these two channels, showing the top atom of the left electrode in transport direction. It shows both $\mathrm{Re}\,\tilde{\boldsymbol{Q}}_1(E)$ and $\mathrm{Re}\,\tilde{\boldsymbol{Q}}_2(E)$ on the dimer atoms. Red are the displacements for eigenchannel 1, blue for eigenchannel 2, and the geometry has been rotated such that the displacement vectors of channel 1 point out of plane. (b) The same as in (a), but for an energy of 10.5 meV. The channel transmissions are $\tau_1 = 0.968$, $\tau_2 = 0.122$, and $\tau_3 = 0.098$. (c) The three highest transmission coefficients as a function of energy for the gold atomic contact shown in (a) and (b). The energies of the eigenchannels considered in these two panels are indicated by arrows, and colored frames around the channel representations serve to identify the corresponding transmission values in (c).

1. Gold dimer contact

The heat conductance of gold atomic contacts has been measured recently [5,6], and we have performed a detailed theoretical analysis of the thermal transport due to both electrons and phonons in these systems [5,59]. We focus here on a gold contact that is one-atom thick and features a dimer in the narrowest part. The geometry, which is shown in Fig. 2, describes junctions with an electrical conductance of the order of the electrical conductance quantum $G_0 = 2e^2/h$. In Figs. 2(a)–2(c) we display the energy-dependent phonon transmission together with eigenchannel representations for two different energies, as indicated by arrows in the transmission plot.

In Fig. 2(a) we show the three eigenchannels with the highest transmission for an energy of 1.5 meV. As one can see, the first two channels correspond to modes with mainly transverse character with respect to the transport direction, whose polarizations are rather perpendicular to each other. For the first channel, with a nearly perfect transmission $\tau_1 \approx 1$, the atomic displacements are almost symmetric on both sides of the junction. In contrast, for the second channel, with a transmission $\tau_2 < 1$, a reduced amplitude is seen on the right part as compared to the left one. This illustrates that the wave coming in from the left is mostly reflected at the central part of the junction. The third channel shows a clearly longitudinal character, and the amplitudes of atomic motion decay even more rapidly from left to right because of the low transmission probability τ_3. Due to the small energy ($E = 1.5$ meV) chosen in this example, the wavelength of atomic motion spans the central part of the junction.

To explore the behavior of the eigenchannels at shorter phonon wavelengths, we show in Fig. 2(b) the three most transmissive eigenchannels for an energy of 10.5 meV. We find that the first mode is of a pronounced longitudinal character at the dimer in the center of the junction, and we see that the dimer atoms often move with opposite velocities, i.e., the out-of-phase character is strongly enhanced as compared to the previous in-phase motion at $E = 1.5$ meV. Let us mention that, as discussed for the 1D model, due to the smaller wavelength of the vibrational modes at $E = 10.5$ meV, the displacements at $t = 0$ are not maximal for all of the atoms, so in order to get a better impression of the modes one has to look at the time-dependent solution in Ref. [57]. For the other two channels at the energy of $E = 10.5$ meV, the amplitudes on the right junction side are, as expected, substantially reduced due to the smaller transmission values τ_2 and τ_3. While the third eigenchannel exhibits predominantly a longitudinal character on the dimer atoms, no clear type can be assigned to the second eigenchannel.

2. Alkane contact

The phonon transport in molecular junctions based on alkane chains has been studied by several theoretical groups employing different methods [22,63–65], and it has also been explored experimentally in the context of many-molecule junctions [66–70]. In Ref. [60] we have studied, in particular, the length dependence of the phononic thermal conductance in single-molecule junctions based on alkane chains. Here, we focus on the analysis of a single-molecule junction containing a dithiolated decane (i.e., an alkane chain with 10 CH_2 segments) coupled to gold leads. In Figs. 3(a)–3(c), we display the energy-dependent transmission together with eigenchannel representations at the two different energies indicated by arrows in the transmission plot. The eigenchannels are furthermore compared to normal modes of the isolated molecule.

In Fig. 3(a) we show the eigenchannels with the three highest transmission coefficients at the energy $E = 7.61$ meV. In addition, we also show two vibrational modes of the free molecule with energies of 6.4 and 9.8 meV. Compared to the axis through the two terminal sulfur atoms, these modes can be described as predominantly transversal, but they can also

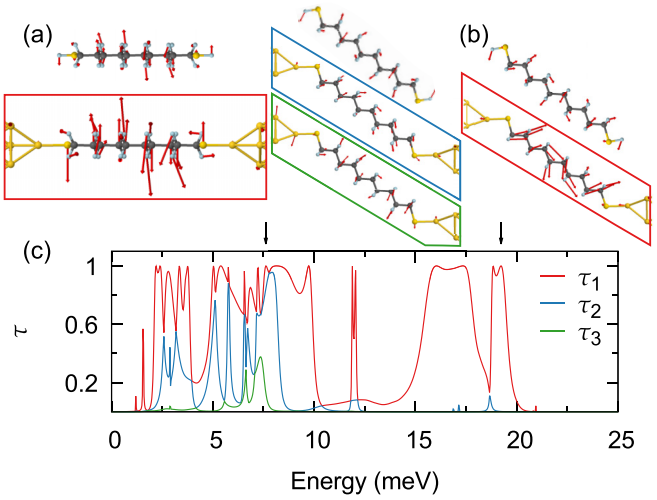

FIG. 3. (a) Transmission eigenchannels for an Au-decane-dithiol-Au junction at an energy of 7.61 meV. We show the three eigenchannels with the highest transmissions of $\tau_1 = 1.00$, $\tau_2 = 0.84$, and $\tau_3 = 0.13$ as well as two vibrational modes of the free molecule at energies of 6.4 and 9.8 meV. (b) The most transmissive eigenchannel at an energy of 19.23 meV and a vibrational mode of the free molecule at energy 18.76 meV. (c) Three highest transmission eigenvalues as a function of energy for the Au-decane-dithiol-Au junction. The energies of the eigenchannels shown in (a) and (b) are indicated with arrows. In these two panels the angle of view differs for modes with out-of-plane as compared to in-plane character.

be classified as out-of-plane and in-plane modes, respectively, if we consider the plane spanned by the molecular backbone of sulfur and carbon atoms. Based on the $t = 0$ snapshot, the first eigenchannel shows some similarities with the first mode of the free molecule at 6.4 meV, both modes having a clear transversal, out-of-plane character and a change of sign with respect to the center of the carbon chain. The other two channels are closely related to a second mode of the free molecule at 9.8 meV, which exhibits a transversal in-plane character and one sign change when going from one end of the carbon chain to the other one. Although the correspondence for the third eigenchannel seems more obvious, the in-plane character and the sign change are clearly visible for the second one, too. Let us mention that we have changed the perspective for all modes and eigenchannels with in-plane character as compared to those with out-of-plane type to better visualize the atomic motions involved.

Further insight into the nature of the eigenchannels can be gained by looking at the full time-dependent solutions [57]. In the movies available in Ref. [57] one can see that the first eigenchannel exhibits the transversal, out-of-plane character that is already apparent in the static representation of Fig. 3(a). For the second and third eigenchannels, the movies reveal similar in-plane atomic motions inside the molecule, but when compared to the sulfur-sulfur axis or those between the two Au tip atoms, they also reveal a partially longitudinal character of the second eigenchannel.

This example shows that an unambiguous identification of the eigenchannels with the modes of the free molecule is not always possible since in the junction the molecule is exposed to different boundary conditions. Mathematically, this is also evident when considering the phase factors related to traveling waves [see the terms $u_n(t, E)$ discussed in Sec. III A], which do not appear in an isolated molecule. Nevertheless, a qualitative relation of the eigenchannels to free modes can sometimes still be seen.

In Fig. 3(b) we display the most transmissive eigenchannel at an energy of 19.23 meV along with a vibrational mode of the free molecule with energy 18.76 meV that exhibits a very similar character. The eigenchannel in this case is mainly of longitudinal, in-plane type, like the free-molecule mode. Note the shorter wavelength of the propagating wave at the higher energy in Fig. 3(b) as compared to Fig. 3(a) in the static representation of the eigenchannel.

3. *Brominated benzene-diamine contact*

Another important example, in which the eigenchannel concept provides a better understanding, is the case when destructive interference effects occur in the phonon transport. We have shown in Ref. [61] that the introduction of substituents in benzene molecules can lead to the appearance of destructive interferences in corresponding single-molecule junctions based on Au electrodes, despite their low Debye energy. The interference effects are reflected in the appearance of antiresonances in the phonon transmission.

In Fig. 4 we show the energy dependence of the three largest eigenchannel transmissions of an Au-2-bromo-1,4-diaminobenzene-Au junction studied in Ref. [61], in which an antiresonance appears at around 19 meV. We have attributed this antiresonance to the interference of the two out-of-plane modes of the free molecule that lie close in energy at 15.61 and 20.07 meV and that are shown in the upper part of Fig. 4. In that figure we also display the most transmissive eigenchannel for three different energies, which dominates the phonon transport. As can be seen, all the eigenchannels exhibit indeed

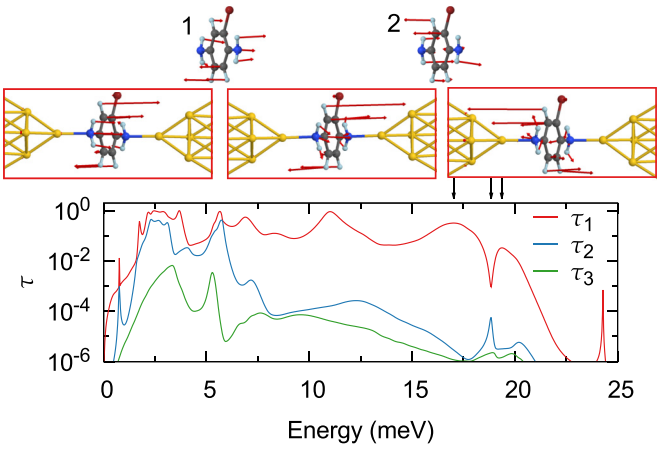

FIG. 4. The three highest eigenchannel transmissions as a function of energy for a Au-2-bromo-1,4-diaminobenzene-Au junction. Above the graph, one can see the eigenchannels with the highest transmission for the three different energies of 17.03, 18.85, and 19.37 meV. The energies are selected by peaks of τ_1 in the transmission plot and are indicated by corresponding arrows. Above the eigenchannels we show the vibrational modes of the free molecule that are responsible for the destructive interference.

a character that resembles the out-of-plane character (with respect to the molecular plane) of the two vibrational modes of the free molecule. Below the interference, one would naively expect the eigenchannel to resemble the first eigenmode of the free molecule, while above it could be related to the second mode of the free molecule. However, and in spite of the fact that the second mode of the free molecule and the highest eigenmode are similar, a simple one-to-one correspondence cannot be established, especially for the first eigenchannel. Again, as in the alkane example, this is partially due to the perturbation of the molecular modes due to the presence of the metal atoms. In addition, since both molecular vibrations are close in energy, the eigenchannel is actually a mixture of both of them with different, non-negligible weights. Moreover, in the static picture of the eigenchannel shown in Fig. 4, one can see a jump of π in the phase of molecular motion as compared to the Au reference atoms, which is reflected by the fact that the arrows on the molecule point in opposite directions at energies above and below the antiresonance. This jump in the phase is a well-known phenomenon that accompanies destructive interference of various properties in the electronic transport [71,72] and, in general, in the Fano model [73].

Our example illustrates how the eigenchannel concept helps to identify the molecular origin of destructive quantum interference. This is particularly useful in cases in which is not easy to figure out the vibrational modes responsible for the interference phenomenon because of the presence of many other modes in that energy region or because the energies of the vibrations of the free molecule are strongly renormalized by the hybridization with the metallic leads when the molecule is connected to the electrodes.

4. C_{60} *contact*

Let us now discuss the case of an Au-C_{60}-Au junction (see Fig. 5), which we have analyzed in Ref. [62] in the context of the thermoelectric figure of merit of fullerene-based junctions. This is a very interesting case because so far we have dealt with molecular junctions where at least one of the modes of the molecule was inside the energy window set by the gold Debye energy. In the C_{60} case, however, all the vibrational modes of the free molecule have energies clearly above that threshold. So, one may wonder how phonon transport can occur in this junction. This can be nicely answered with the help of the transmission eigenchannels.

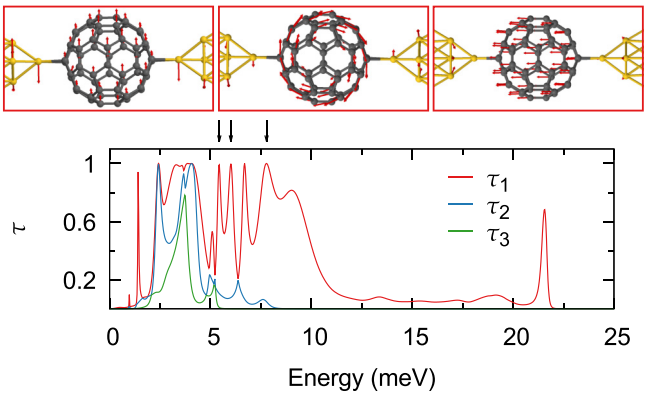

FIG. 5. The three largest transmission coefficients for a Au-C_{60}-Au junction as a function of energy. The most transmissive eigenchannels at energies of 5.4, 6.0, and 7.8 meV, as indicated by arrows in the transmission plot, are shown in the upper part of the figure.

For this purpose, we present in Fig. 5 the most transmissive eigenchannels at energies of 5.4, 6.0, and 7.8 meV above a plot of the energy-dependent transmission. As one can see, all the eigenchannels correspond to a hybridization of the vibrations of the gold atoms with the center-of-mass motion of the C_{60} molecule. The eigenchannel at 5.4 meV possesses a transversal character, where the molecule moves up and down as a whole, and it also involves transversal motions of the gold atoms in the electrode tips. The eigenchannel at 6.0 meV involves a rotation of the molecule that is again coupled to transversal vibrations of the gold atoms. Finally, the eigenchannel at 7.8 meV involves a longitudinal center-of-mass motion of the C_{60} that is coupled to a predominantly longitudinal movement of the Au tip atoms. Let us point out that in the movies of the eigenchannels, a small deformation of the C_{60} molecule can also be seen in all three examples in addition to the main center-of-mass motion highlighted by the static pictures [57].

IV. CONCLUSIONS

In this work, and in analogy with what is done in electronic transport, we have presented a method to obtain the transmission eigenchannels from NEGF-based calculations of the coherent phonon transport. In particular, we have shown that this method can be combined with *ab initio* simulations to provide an insight into phonon transport that cannot simply be obtained from the analysis of the transmission probabilities. We have illustrated this approach with the analysis of the phonon eigenchannels in realistic atomic-scale junctions, including single-atom and single-molecule junctions. Moreover, we have discussed different ways to visualize these eigenchannels by means of static and time-dependent representations. We believe that the procedure presented in this work will become a valuable tool for the analysis of coherent phonon transport in a great variety of nanoscale systems and devices.

ACKNOWLEDGMENTS

J.C.K. and F.P. thank M. Bürkle for stimulating discussions in the initial phase of this work. In addition, both gratefully acknowledge funding from the Carl Zeiss foundation, the Junior Professorship Program of the Ministry of Science, Research and the Arts of the state of Baden Württemberg, and the Collaborative Research Center (SFB) 767 of the German Research Foundation (DFG). J.C.C. thanks the Spanish Ministry of Economy and Competitiveness (Contract No. FIS2017-84057-P) for financial support as well as the DFG and SFB 767 for sponsoring his stay at the University of Konstanz as Mercator Fellow. An important part of the numerical modeling was carried out on the computational resources of the bwHPC program, namely, the bwUniCluster and the JUSTUS HPC facility.

[1] D. G. Cahill, W. K. Ford, K. E. Goodson, G. D. Mahan, A. Majumdar, H. J. Maris, R. Merlin, and S. R. Phillpot, Nanoscale thermal transport, J. Appl. Phys. **93**, 793 (2003).

[2] E. Pop, Energy dissipation and transport in nanoscale devices, Nano Res. **3**, 147 (2010).

[3] T. Luo and G. Chen, Nanoscale heat transfer - from computation to experiment, Phys. Chem. Chem. Phys. **15**, 3389 (2013).

[4] D. G. Cahill, P. V. Braun, G. Chen, D. R. Clarke, S. Fan, K. E. Goodson, P. Keblinski, W. P. King, G. D. Mahan, A. Majumdar, H. J. Maris, S. R. Phillpot, E. Pop, and L. Shi, Nanoscale thermal transport. II. 2003–2012, Appl. Phys. Rev. **1**, 011305 (2014).

[5] L. Cui, W. Jeong, S. Hur, M. Matt, J. C. Klöckner, F. Pauly, P. Nielaba, J. C. Cuevas, E. Meyhofer, and P. Reddy, Quantized thermal transport in single-atom junctions, Science **355**, 1192 (2017).

[6] N. Mosso, U. Drechsler, F. Menges, P. Nirmalraj, S. Karg, H. Riel, and B. Gotsmann, Heat transport through atomic contacts, Nat. Nanotechnol. **12**, 430 (2017).

[7] A. J. Minnich, Advances in the measurement and computation of thermal phonon transport properties, J. Phys.: Condens. Matter **27**, 053202 (2015).

[8] J. C. Cuevas and E. Scheer, *Molecular Electronics: An Introduction to Theory and Experiment*, 2nd ed. (World Scientific, Singapore, 2017).

[9] D. Segal and B. K. Agarwalla, Vibrational heat transport in molecular junctions, Annu. Rev. Phys. Chem. **67**, 185 (2016).

[10] G. Fagas, A. G. Kozorezov, C. J. Lambert, J. K. Wigmore, A. Peacock, A. Poelaert, and R. den Hartog, Lattice dynamics of a disordered solid-solid interface, Phys. Rev. B **60**, 6459 (1999).

[11] H. Zhao and J. B. Freund, Lattice-dynamical calculation of phonon scattering at ideal Si-Ge interfaces, J. Appl. Phys. **97**, 024903 (2005).

[12] J. Wang and J.-S. Wang, Mode-dependent energy transmission across nanotube junctions calculated with a lattice dynamics approach, Phys. Rev. B **74**, 054303 (2006).

[13] I. Duchemin and D. Donadio, Atomistic calculation of the thermal conductance of large scale bulk-nanowire junctions, Phys. Rev. B **84**, 115423 (2011).

[14] L. Zhang, P. Keblinski, J.-S. Wang, and B. Li, Interfacial thermal transport in atomic junctions, Phys. Rev. B **83**, 064303 (2011).

[15] Y. Tanaka, F. Yoshida, and S. Tamura, Lattice thermal conductance in nanowires at low temperatures: Breakdown and recovery of quantization, Phys. Rev. B **71**, 205308 (2005).

[16] V. B. Antonyuk, M. Larsson, A. G. Mal'shukov, and K. A. Chao, Phonon transmission in III-V semiconductor superlattices and alloys, Semicond. Sci. Technol. **20**, 347 (2005).

[17] P. G. Murphy and J. E. Moore, Coherent phonon scattering effects on thermal transport in thin semiconductor nanowires, Phys. Rev. B **76**, 155313 (2007).

[18] N. Mingo and L. Yang, Phonon transport in nanowires coated with an amorphous material: An atomistic Green's function approach, Phys. Rev. B **68**, 245406 (2003).

[19] N. Mingo, Anharmonic phonon flow through molecular-sized junctions, Phys. Rev. B **74**, 125402 (2006).

[20] Y. Asai, Nonequilibrium phonon effects on transport properties through atomic and molecular bridge junctions, Phys. Rev. B **78**, 045434 (2008).

[21] T. Markussen, Phonon interference effects in molecular junctions, J. Chem. Phys. **139**, 244101 (2013).

[22] H. Sadeghi, S. Sangtarash, and C. J. Lambert, Oligoyne molecular junctions for efficient room temperature thermoelectric power generation, Nano Lett. **15**, 7467 (2015).

[23] M. Bürkle, T. J. Hellmuth, F. Pauly, and Y. Asai, First-principles calculation of the thermoelectric figure of merit for [2,2]paracyclophane-based single-molecule junctions, Phys. Rev. B **91**, 165419 (2015).

[24] Q. Li, I. Duchemin, S. Xiong, G. C. Solomon, and D. Donadio, Mechanical tuning of thermal transport in a molecular junction, J. Phys. Chem. C **119**, 24636 (2015).

[25] Q. Li, M. Strange, I. Duchemin, D. Donadio, and G. C. Solomon, A strategy to suppress phonon transport in molecular junctions using π-stacked systems, J. Phys. Chem. C **121**, 7175 (2017).

[26] M. Buerkle and Y. Asai, Thermal conductance of teflon and polyethylene: Insight from an atomistic, single-molecule level, Sci. Rep. **7**, 41898 (2017).

[27] M. Famili, I. Grace, H. Sadeghi, and C. J. Lambert, Suppression of phonon transport in molecular Christmas trees, Chem. Phys. Chem. **18**, 1234 (2017).

[28] J.-S. Wang, J. Wang, and J. T. Lü, Quantum thermal transport in nanostructures, Eur. Phys. J. B **62**, 381 (2008).

[29] M. Brandbyge, M. R. Sørensen, and K. W. Jacobsen, Conductance eigenchannels in nanocontacts, Phys. Rev. B **56**, 14956 (1997).

[30] J. C. Cuevas, A. Levy Yeyati, and A. Martín-Rodero, Microscopic Origin of Conducting Channels in Metallic Atomic-Size Contacts, Phys. Rev. Lett. **80**, 1066 (1998).

[31] E. Scheer, N. Agraït, J. C. Cuevas, A. L. Yeyati, B. Ludoph, A. Mart-Rodero, G. R. Bollinger, J. M. van Ruitenbeek, and C. Urbina, The signature of chemical valence in the electrical conduction through a single-atom contact, Nature (London) **394**, 154 (1998).

[32] N. Agraït, A. L. Yeyati, and J. M. van Ruitenbeek, Quantum properties of atomic-sized conductors, Phys. Rep. **377**, 81 (2003).

[33] E. Scheer, P. Joyez, D. Esteve, C. Urbina, and M. H. Devoret, Conduction Channel Transmissions of Atomic-Size Aluminum Contacts, Phys. Rev. Lett. **78**, 3535 (1997).

[34] E. Scheer, W. Belzig, Y. Naveh, M. H. Devoret, D. Esteve, and C. Urbina, Proximity Effect and Multiple Andreev Reflections in Gold Atomic Contacts, Phys. Rev. Lett. **86**, 284 (2001).

[35] C. Schirm, M. Matt, F. Pauly, J. C. Cuevas, P. Nielaba, and E. Scheer, A current-driven single-atom memory, Nat. Nanotechnol. **8**, 645 (2013).

[36] H. E. van den Brom and J. M. van Ruitenbeek, Quantum Suppression of Shot Noise in Atom-Size Metallic Contacts, Phys. Rev. Lett. **82**, 1526 (1999).

[37] R. Cron, M. F. Goffman, D. Esteve, and C. Urbina, Multiple-Charge-Quanta Shot Noise in Superconducting Atomic Contacts, Phys. Rev. Lett. **86**, 4104 (2001).

[38] D. Djukic and J. M. van Ruitenbeek, Shot noise measurements on a single molecule, Nano Lett. **6**, 789 (2006).

[39] M. Kiguchi, O. Tal, S. Wohlthat, F. Pauly, M. Krieger, D. Djukic, J. C. Cuevas, and J. M. van Ruitenbeek, Highly Conductive Molecular Junctions Based on Direct Binding of Benzene to Platinum Electrodes, Phys. Rev. Lett. **101**, 046801 (2008).

[40] R. Vardimon, M. Klionsky, and O. Tal, Experimental determination of conduction channels in atomic-scale conductors based on shot noise measurements, Phys. Rev. B **88**, 161404 (2013).

[41] M. A. Karimi, S. G. Bahoosh, M. Herz, R. Hayakawa, F. Pauly, and E. Scheer, Shot noise of 1,4-benzenedithiol single-molecule junctions, Nano Lett. **16**, 1803 (2016).

[42] Z.-Y. Ong and G. Zhang, Efficient approach for modeling phonon transmission probability in nanoscale interfacial thermal transport, Phys. Rev. B **91**, 174302 (2015).

[43] S. Sadasivam, U. V. Waghmare, and T. S. Fisher, Phonon-eigenspectrum-based formulation of the atomistic Green's function method, Phys. Rev. B **96**, 174302 (2017).

[44] Z.-X. Xie, K.-Q. Chen, and W. Duan, Thermal transport by phonons in zigzag graphene nanoribbons with structural defects, J. Phys.: Condens. Matter **23**, 315302 (2011).

[45] J. Wang, L. Li, and J.-S. Wang, Tuning thermal transport in nanotubes with topological defects, Appl. Phys. Lett. **99**, 091905 (2011).

[46] T. Ouyang, Y. Chen, L.-M. Liu, Y. Xie, X. Wei, and J. Zhong, Thermal transport in graphyne nanoribbons, Phys. Rev. B **85**, 235436 (2012).

[47] X.-F. Peng and K.-Q. Chen, Thermal transport for flexural and in-plane phonons in graphene nanoribbons, Carbon **77**, 360 (2014).

[48] M. Paulsson and M. Brandbyge, Transmission eigenchannels from nonequilibrium Green's functions, Phys. Rev. B **76**, 115117 (2007).

[49] M. Bürkle, J. K. Viljas, D. Vonlanthen, A. Mishchenko, G. Schön, M. Mayor, T. Wandlowski, and F. Pauly, Conduction mechanisms in biphenyl dithiol single-molecule junctions, Phys. Rev. B **85**, 075417 (2012).

[50] J. E. G. Farina, *Quantum Theory of Scattering Processes (The International Encyclopedia of Physical Chemistry and Chemical Physics. Topic 2: Classical and Quantum Mechanics, Vol. 4)*, 1st ed. (Pergamon Press, Oxford, 1973).

[51] W. Zhang, T. S. Fisher, and N. Mingo, The atomistic Green's function method: An efficient simulation approach for nanoscale phonon transport, Numer. Heat Transfer, Part B **51**, 333 (2007).

[52] J.-S. Wang, J. Wang, and N. Zeng, Nonequilibrium Green's function approach to mesoscopic thermal transport, Phys. Rev. B **74**, 033408 (2006).

[53] J.-S. Wang, N. Zeng, J. Wang, and C. K. Gan, Nonequilibrium Green's function method for thermal transport in junctions, Phys. Rev. E **75**, 061128 (2007).

[54] T. Yamamoto and K. Watanabe, Nonequilibrium Green's Function Approach to Phonon Transport in Defective Carbon Nanotubes, Phys. Rev. Lett. **96**, 255503 (2006).

[55] J.-S. Wang, B. K. Agarwalla, H. Li, and J. Thingna, Nonequilibrium Green's function method for quantum thermal transport, Front. Phys. **9**, 673 (2014).

[56] S. G. Das and A. Dhar, Landauer formula for phonon heat conduction: Relation between energy transmittance and transmission coefficient, Eur. Phys. J. B **85**, 372 (2012).

[57] See Supplemental Material at http://link.aps.org/supplemental/10.1103/PhysRevB.97.155432 for additional information regarding the 1D chain and video files showing time-dependent representations of the eigenchannels of each atomic and molecular junction.

[58] N. W. Ashcroft and N. Mermin, *Solid State Physics* (Hartcourt, Orlando, 1976).

[59] J. C. Klöckner, M. Matt, P. Nielaba, F. Pauly, and J. C. Cuevas, Thermal conductance of metallic atomic-size contacts: Phonon transport and Wiedemann-Franz law, Phys. Rev. B **96**, 205405 (2017).

[60] J. C. Klöckner, M. Bürkle, J. C. Cuevas, and F. Pauly, Length dependence of the thermal conductance of alkane-based single-molecule junctions: An *ab initio* study, Phys. Rev. B **94**, 205425 (2016).

[61] J. C. Klöckner, J. C. Cuevas, and F. Pauly, Tuning the thermal conductance of molecular junctions with interference effects, Phys. Rev. B **96**, 245419 (2017).

[62] J. C. Klöckner, R. Siebler, J. C. Cuevas, and F. Pauly, Thermal conductance and thermoelectric figure of merit of C_{60}-based single-molecule junctions: Electrons, phonons, and photons, Phys. Rev. B **95**, 245404 (2017).

[63] D. Segal, A. Nitzan, and P. Hänggi, Thermal conductance through molecular wires, J. Chem. Phys. **119**, 6840 (2003).

[64] T. Luo and J. R. Lloyd, Non-equilibrium molecular dynamics study of thermal energy transport in Au-SAM-Au junctions, Int. J. Heat Mass Transfer **53**, 1 (2010).

[65] J. C. Duda, C. B. Saltonstall, P. M. Norris, and P. E. Hopkins, Assessment and prediction of thermal transport at solid-self-assembled monolayer junctions, J. Chem. Phys. **134**, 094704 (2011).

[66] R. Y. Wang, R. A. Segalman, and A. Majumdar, Room temperature thermal conductance of alkanedithiol self-assembled monolayers, Appl. Phys. Lett. **89**, 173113 (2006).

[67] Z. Wang, J. A. Carter, A. Lagutchev, Y. K. Koh, N.-H. Seong, D. G. Cahill, and D. D. Dlott, Ultrafast flash thermal conductance of molecular chains, Science **317**, 787 (2007).

[68] M. D. Losego, M. E. Grady, N. R. Sottos, D. G. Cahill, and P. V. Braun, Effects of chemical bonding on heat transport across interfaces, Nat. Mater. **11**, 502 (2012).

[69] T. Meier, F. Menges, P. Nirmalraj, H. Hölscher, H. Riel, and B. Gotsmann, Length-Dependent Thermal Transport along Molecular Chains, Phys. Rev. Lett. **113**, 060801 (2014).

[70] S. Majumdar, J. A. Sierra-Suarez, S. N. Schiffres, W.-L. Ong, C. F. Higgs, A. J. H. McGaughey, and J. A. Malen, Vibrational mismatch of metal leads controls thermal conductance of self-assembled monolayer junctions, Nano Lett. **15**, 2985 (2015).

[71] G. C. Solomon, C. Herrmann, T. Hansen, V. Mujica, and M. A. Ratner, Exploring local currents in molecular junctions, Nat. Chem. **2**, 223 (2010).

[72] G. C. Solomon, D. Q. Andrews, T. Hansen, R. H. Goldsmith, M. R. Wasielewski, R. P. Van Duyne, and M. A. Ratner, Understanding quantum interference in coherent molecular conduction, J. Chem. Phys. **129**, 054701 (2008).

[73] Y. S. Joe, A. M. Satanin, and C. S. Kim, Classical analogy of Fano resonances, Phys. Scr. **74**, 259 (2006).